Provided for non-commercial research and education use.
Not for reproduction, distribution or commercial use.

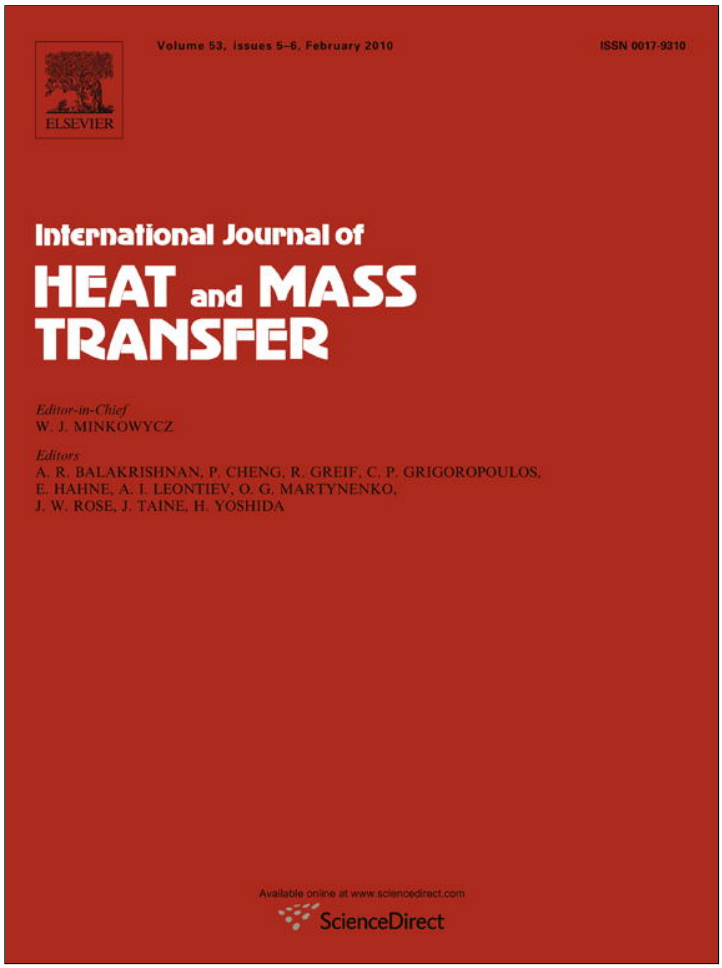

This article appeared in a journal published by Elsevier. The attached copy is furnished to the author for internal non-commercial research and education use, including for instruction at the authors institution and sharing with colleagues.

Other uses, including reproduction and distribution, or selling or licensing copies, or posting to personal, institutional or third party websites are prohibited.

In most cases authors are permitted to post their version of the article (e.g. in Word or Tex form) to their personal website or institutional repository. Authors requiring further information regarding Elsevier's archiving and manuscript policies are encouraged to visit:

http://www.elsevier.com/copyright

Author's personal copy

International Journal of Heat and Mass Transfer 53 (2010) 1100–1111

Contents lists available at ScienceDirect

International Journal of Heat and Mass Transfer

journal homepage: www.elsevier.com/locate/ijhmt

Droplet evaporation characteristics due to wet compression under RCM conditions

M.V. Johnson [a], G.S. Zhu [b,1], S.K. Aggarwal [c,2], S.S. Goldsborough [a,*]

[a] Department of Mechanical Engineering, Marquette University, P.O. Box 1881, Milwaukee, WI 53201-1881, USA
[b] HDEP Performance and Emissions, DTNA – Detroit Diesel Corporation, 13400 Outer Dr., West Detroit, MI 48239, USA
[c] Department of Mechanical and Industrial Engineering, University of Illinois at Chicago, 1030 Engineering Research Facility, 842 W. Taylor Street, Chicago, IL 60607, USA

ARTICLE INFO

Article history:
Received 22 April 2009
Accepted 27 October 2009
Available online 11 December 2009

Keywords:
Wet compression
Droplet evaporation
Aerosol RCM

ABSTRACT

The vaporization characteristics of a single fuel droplet subjected to rapid gas-phase compression (i.e., wet compression) are computationally investigated using two spherically-symmetric models: quasi-steady (QS) and fully transient (TS). Features of the wet compression process under rapid compression machine (RCM) conditions are discussed with these compared to simulations where the far-field conditions are essentially invariant. It is observed that wet compression can significantly increase the rate of evaporation primarily due to the increase in droplet temperature and corresponding saturation pressure (fugacity); an increase in the density-weighted mass diffusivity is also beneficial in reducing the droplet consumption times. The QS model predicts substantially longer rates of evaporation relative to the TS model due to transient behavior associated with the initial evaporative cooling process, and the gas-phase compression heating process. Increases in the rate of volumetric compression can lead to more rapid droplet consumption, however there is a corresponding increase in spatial stratification in the gas- and liquid-phases which may not be advantageous for RCM applications. An 'operating map' has been developed based on parametric simulations of an *n*-dodecane droplet evaporating into nitrogen.

© 2009 Elsevier Ltd. All rights reserved.

1. Introduction

Wet compression is the process whereby droplet evaporation is achieved through compression heating of the gas-phase of a droplet laden aerosol. This phenomenon has received increasing attention in recent years with applications to internal combustion (IC) and gas turbine (GT) engines, as well as laboratory devices such as aerosol shock tubes (STs) and rapid compression machines (RCMs). In advanced IC engines non-conventional combustion strategies are being investigated in order to reduce soot, NO_x and unburned hydrocarbon (UHC) emissions while maintaining high energy conversion efficiencies [1–5]. In these, sometimes referred to as low temperature combustion (LTC) schemes, the fuel can be introduced very early in the compression stroke, in some cases well in advance of maximum piston compression. Under such conditions the in-cylinder gases are relatively cool, meaning they may be at or below the fuel's boiling point (e.g., $T_b \sim 650$ K). During the piston's compression stroke the liquid droplets are vaporized due to the gas-phase volumetric compression, and the fuel vapor is subsequently mixed with the gas-phase oxidizer. Droplet coalescence and wall wetting during compression, especially important for highly involatile fuels or fuel components, can lead to extended evaporation times and the formation of unwanted emissions [6]. Wet compression is also important in IC engines that utilize "wet" ethanol, which is a minimally-processed ethanol-based fuel with high water content [7]. In these engines much of the ethanol readily evaporates during the induction stroke however, the water may not completely vaporize until well into the compression stroke.

In GT engines wet compression of water aerosols has been used to achieve "continuous cooling" in the compressor component of the engine [8–13]. In engines employing this process, water droplets with diameters on the order of ~15 μm are injected into the intake stream via fogging systems with high droplet output. The pressure-driven injectors used in these systems achieve very high relative droplet–air velocities and rapid mixing of the evolving water vapor with the air. This can result in significantly increased power densities along with cost and performance advantages relative to conventional inter-cooling units. However, it is only effective when the humidity ratio of the intake air is low and the residence time in the compressor is adequate to achieve complete evaporation.

In shock tubes (STs) and rapid compression machines (RCMs) wet compression has been proposed as a means of preparing test gases of high molecular weight (MW), involatile liquid fuels relevant to the transportation industry. Traditional charge preparation techniques use external mixing protocols based on partial pressure methodologies [14,15]. Diesel-representative fuels for example,

* Corresponding author. Tel.: +1 414 288 6641; fax: +1 414 288 7790.
E-mail address: scott.goldsborough@mu.edu (S.S. Goldsborough).
[1] Tel.: +1 313 592 5896; fax: +1 313 592 5906.
[2] Tel.: +1 312 413 9712; fax: +1 312 413 0447.

0017-9310/$ - see front matter © 2009 Elsevier Ltd. All rights reserved.
doi:10.1016/j.ijheatmasstransfer.2009.10.047

Author's personal copy

Nomenclature

B	mass transfer number
c_p	specific heat at constant pressure
c_v	specific heat at constant volume
D	mass diffusion coefficient
d	diameter
D_{sm}	Sauter mean diameter
h	specific enthalpy
H	thermal energy supplied
I	specific internal energy
L	heat of vaporization
Le	Lewis number (κ/D)
$\dot{m}$	mass flow rate
$\bar{m}$	non-dimensional mass flow rate, $\dot{m}/4\pi\rho_g D_g r_g$
N	total number of species in the mixture
P	pressure
r	radial direction
$\bar{r}$	non-dimensional radius, r/r_s
R	ideal gas constant
Re	Reynolds number, $\rho u D/\mu$
t	time
$\bar{t}$	non-dimensional time, $\int \hat{\kappa}_l dt/r_s^2$
T	temperature
$\bar{T}$	non-dimensional temperature, T/T_{ref}
u	velocity
V	volume
X	mass fraction, liquid phase
Y	mass fraction, vapor phase
z	compressibility factor

Greeks

α	thermal conductivity
γ	ratio of specific heats, c_p/c_v
κ	heat diffusivity
λ	second viscosity coefficient
μ	dynamic viscosity
ρ	density
υ	specific volume
ϕ	fugacity coefficient

Subscripts

avg	average
b	boiling
c	critical point property
f	fuel
g	gas-phase
i	ith species
ii	iith cell
inst	instantaneous
j	jth species
k	kth species
l	liquid-phase
s	surface
0	initial condition
∞	far-field condition

have very low vapor pressures at standard conditions (e.g., <1 Torr) which make this option difficult or impossible. Heating the mixing tanks and equipment can lead to better fuel vaporization but this can result in seal degradation issues in RCMs, as well as concern for pre-test reactivity during the preparation process. Aerosols of suspended fuel droplets (Sauter mean diameter, $D_{sm} \sim 8$–18 μm) have been used to deliver liquid fuels to the machines where subsequent compression of the surrounding gas phase leads to evaporation of the liquid fuel droplets [16,17]. In shock tubes where test temperatures range from 900 to 2000 K the gas-phase compression event is achieved via a rapidly traveling shock wave (compression achieved in ~30 μs to 600–700 K); the passing of the initial wave not only increases the pressure and temperature of the surrounding bath gases but it fragments the initial droplets and results in high convective velocities near the droplet surface (which enhances vaporization). The subsequent reflected wave compresses the evaporated mixture to the test conditions. In RCMs where test temperatures are generally between 600 and 1100 K the compression event is much slower (e.g., ~15–60 ms) and the bulk gas motion is often suppressed in order to minimize unwanted heat loss during the test period [17]. Droplet evaporation is much slower and is mainly diffusion-limited. Evaporation must also be achieved at lower temperatures, i.e., before the test temperature is reached.

2. Background

The design and operation of devices that can effectively utilize the wet compression process requires a fundamental understanding of droplet evaporation including vapor-phase mixing, diffusion, and saturation phenomena, along with a reasonably accurate means of simulating it with an integrated gas-phase compression model. Droplet evaporation models have a long history of development (e.g., see Refs. [18–20]) and include a number of approaches. Some assume that the bulk gas is stagnate with the gas-phase transport diffusion/Stefan flow limited (i.e., $Re = 0$), while others assume a convective bulk gas flow with an associated Reynolds number (Re). Both quasi-steady (QS) [21–24] and fully transient (TS) [25–29] continuum models have been formulated, which generally utilize the assumption of liquid–vapor equilibria at the droplet–gas interface; other means of prescribing the interface conditions are also possible however (e.g., see Ref. [30]). The quasi-steady approach assumes that the gas-phase transport of heat, mass and momentum is sufficiently fast so that transients within the gas-phase can be ignored relative to the transients associated with the liquid-phase, including the rate of surface regression of the droplet. The fully transient approach does not make this assumption and has been demonstrated to be better suited to resolve evaporation within high pressure environments (e.g., $P > 10$ bar) where gas-phase heat and mass transport can be reduced relative to atmospheric conditions. Both approaches can incorporate various levels of complexity including an accounting of thermal gradients within the droplets, allowance of multiple constituents within the liquid phase, the use of real gas models for thermodynamic and transport properties, and the capability to transition between sub- and supercritical evaporation, among others.

The integration of droplet evaporation models with models for the gas-phase compression process has been attempted in a number of ways. Work to date has focused primarily on GT engine applications and has predominantly employed the quasi-steady approach; examples can be found in Refs. [31–38]. In these integrated models the droplets have been assumed to be uniform in temperature and composition, and the far-field ("mean-line") gas-phase temperature has been modeled as homogeneous but unsteady. Effects of compression heating and bulk gas flow on droplet evaporation rates have been investigated, as have effects of evaporation on gas-phase cooling. Compressor operating maps accounting for ambient humidity and extent of liquid water injection have

Author's personal copy

been an outcome of these studies where increases in power density and outlet temperature are predicted [38].

In addition to GT engine applications, Liu et al. [39] have studied the wet compression process in reference to IC engine applications. They employed a quasi-steady evaporation model assuming a uniform droplet temperature with constant properties and ideal gas behavior. A realistic piston trajectory was used and they investigated the effects of compression ratio, piston speed, initial ambient fuel concentration and temperature on the droplet evaporation characteristics. In that work the far-field temperature and composition were unaffected by the fuel evaporation; in other words, a single droplet was modeled. Liu et al. concluded that opposing effects of increased pressure (i.e., reduced fuel concentration at the droplet surface due to Rault's law, $X_f P = P_f^{sat}(T_s)$) and increased temperature (i.e., higher saturation pressure, $P_f^{sat}(T_s)$) have roughly cancelling effects during the evaporation process. In their calculations there was only slight deviation from d^2-law behavior.

Sheu and Liou [40] also investigated wet compression considering a single liquid droplet exposed to a compressed gas phase. They, however, employed a transient evaporation model, and assumed adiabatic compression where this was specified as a linearly increasing pressure/temperature function. This linear function is not representative of turbine-, or piston-driven volumetric compression where the pressure history is highly nonlinear (as seen in Fig. 1). In addition, the pressure rise rate and total pressure increase are large in operating engines and RCMs (e.g., ~1000 atm/s, $\Delta P \sim 10$–20 bar for typical RCMs (see Fig. 1)), whereas Sheu and Liou used values near 0.15 atm/s and $\Delta P \sim 2$ bar, respectively. In Ref. [40] thermal gradients within the droplets are taken into account, while the properties were assumed to be constant. Uniform pressure was assumed throughout the domain and the ideal gas equation of state (EOS) was used for the gas-phase; viscous transport of heat was ignored in their model. In contrast to the Liu et al. study [39], Sheu and Liou found that droplet evaporation times can be significantly reduced with increasing values of dP/dt, while the extent of reduction is dependent on the droplet and environment conditions (e.g., initial size, temperature, far-field concentration, etc.). They concluded that this is a result of increased saturation pressure due to higher droplet temperatures that result from compression heating.

The objectives of this study are to build upon previous efforts to understand and simulate the wet compression process, and to resolve discrepancies seen between earlier modeling studies. While the model and methodology used are relevant to all of the systems discussed above, the focus here is on RCM applications, and therefore RCM-relevant rates of compression are used. Variations in liquid- and gas-phase properties are taken into account due to the large changes in temperature and pressure seen in some of the simulations. Both quasi-steady and transient evaporation models are used in this work in order to investigate the effects of gas-phase transients on the evaporation process, especially near the droplet. The remainder of this paper is organized as follows. First, an overview of the evaporation models is presented along with a brief discussion of modifications undertaken for this study. Simulation results are then presented which cover a range of initial conditions including temperature, pressure and droplet size, as well as rate of compression. Differences between results of the QS and TS approaches are highlighted and discussed. Finally, an operating map is drawn for an aerosol RCM that summarizes the simulation results and indicates a window for successful operation.

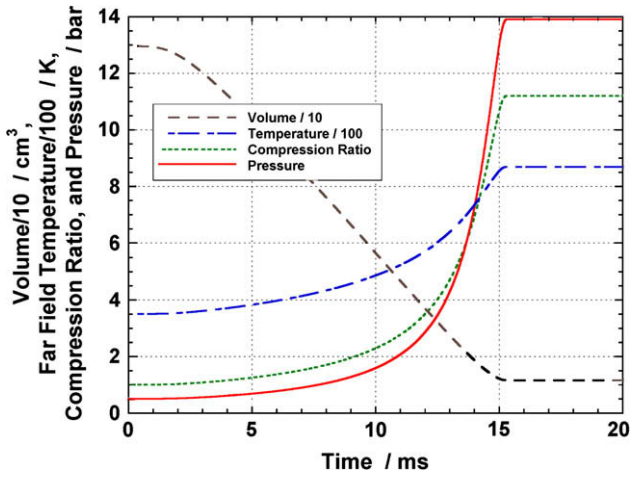

Fig. 1. Representative volume, compression ratio, far-field temperature and pressure histories used in this study where the volume data is typical of rapid compression machines described in the literature, and the far-field temperature and pressure are computed assuming an isentropic compression process from $T_0 = 350$ K and $P_0 = 1$ bar, respectively.

3. Methodology

The evaporation models used in this study are based on work by Aggarwal and co-workers [21,28]. The software utilize a continuum formulation (i.e., phase equilibrium is prescribed at the gas–liquid interface), assume a spherically symmetric droplet, and account for thermal and concentration gradients within the droplet. Pressure variations across the computational domain are taken into account in the transient model. The QS model has been modified in order to account for changes in the liquid-phase properties due to compression heating; these changes alter the calculations for temperature distribution within the droplet, and the surface regression rate. A mesh compression operation has been incorporated into both QS and TS models in order to simulate the gas-phase compression heating process. The operation accounts for the induced convection flow towards the droplet due to volumetric compression. This feature has not been included in previous work, but for highly compressed conditions this is found to be important. Both models assume that a droplet is isolated, i.e., $r_\infty \sim 400^* r_{s,0}$, so that effects of far-field fuel saturation and evaporative cooling (which are important for high aerosol density conditions (e.g., stoichiometric fuel:air ratios)) are ignored. These effects will be investigated in a forthcoming study. The base models have been detailed previously in Refs. [21,22,24,26–29] where predictions have been validated against a range of experimental data. The evaporation models are summarized in Appendices A and B while the accompanying thermo-physical models are discussed in Appendix C.

4. Simulation results

The results presented here are for *n*-dodecane droplets evaporating into nitrogen. *n*-dodecane is a very low volatility ($P^{sat} < 1$ Torr, $T_b = 488$ K @ STP) normal alkane that has been used as a single component surrogate to represent the fundamental features of diesel fuel ignition. It was selected for this study in order to better understand the features of wet compression as it might be applied within an aerosol RCM. Experimental data for ρ, c_p, etc. for *n*-dodecane can be found in Appendix C where these data are compared to the thermo-physical models used in this work. For all of the simulations conducted the droplet and surrounding gas are assumed to be initially in thermal and mechanical equilibrium (i.e., uniform temperature and pressure throughout), with the liquid phase containing only *n*-dodecane and the gas phase only nitrogen.

Author's personal copy

A piston trajectory for a typical RCM is used to specify the time-varying volume of the computational mesh. The trajectory is representative of designs discussed in recent literature where compression times are on the order of 15–25 ms with compression ratios ranging from 11 to 35 [41–43]. For this study the trajectory has been normalized so that any maximum compression ratio, $CR_{max} = V_0/V_{min}$, can be prescribed along with a desired compression time; for the simulation results presented here CR_{max} has been set to 11.2 and t_{comp} nominally to 15.3 ms. The volume trace is illustrated in Fig. 1 along with associated curves for the far-field (i.e., isentropic) temperature and pressure and the instantaneous compression ratio ($CR = V_0/V_{inst}$). In this figure an initial temperature and pressure of 350 K and 0.5 bar, respectively are used where a peak temperature and pressure of 860 K and 13.9 bar, respectively, results. Evident here is that the pressure rise of the gas-phase is most significant during the later stage of the compression process; the rise in temperature follows a similar trend, however this curve is not as steep. The ignition delay time for a stoichiometric mixture of *n*-dodecane/air at the peak compressed conditions is on the order of 2.5 ms, based on the detailed chemical kinetic model of Westbrook et al. [44]. It should be noted that although the TS model accounts for variations in P across the computational domain, for all of the conditions explored here the pressure is found to be uniform, and identical to the QS model.

Figs. 2–7 illustrate results from a series of simulations where the modified QS and TS evaporation models have been used. Fig. 2 presents droplet diameters plotted as a function of time for four initial droplet diameters (1, 4, 11 and 18 μm) at an initial temperature of 350 K and an initial pressure of 1 bar. In addition one higher and one lower temperature, 300 and 380 K, respectively, are used for the $d_0 = 4$ μm droplet. For the smallest and the hottest droplets the evaporation process is computed to be fast enough so that there are no significant effects of the gas-phase compression on the droplet evaporation, i.e., the droplets evaporate before the gas-phase is substantially compressed. These droplets follow d^2-law behavior. For the largest and the coldest droplets however, it can be seen that there are significant effects of gas-phase compression where the evaporation times are substantially reduced relative to uncompressed evaporation. This is due to the increase in droplet temperature and corresponding saturation pressure (fugacity) that result from the gas-phase compression heating; this

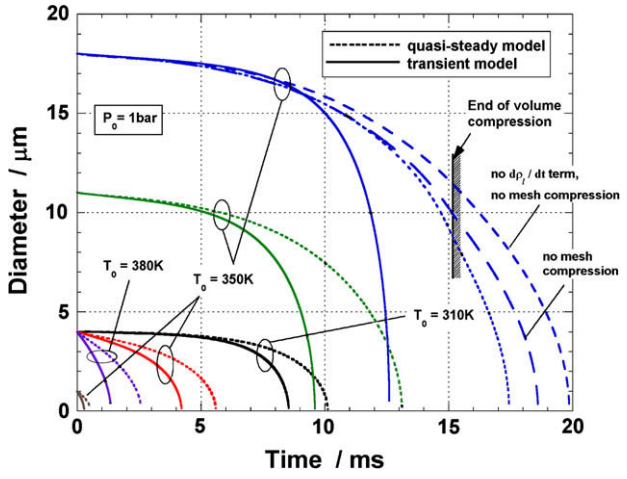

Fig. 2. Droplet diameters as a function of time for various sized droplets at an initial temperature and pressure of 350 K and 1 bar, respectively; diameter histories for two droplets initially at $d_0 = 4$ μm, $P_0 = 1$ bar, and 310 K and 380 K are also shown. Differences in predictions for the QS and TS evaporation models are visible, as are the effects of accounting for droplet property transients and the mesh compression operation in the modified quasi-steady model.

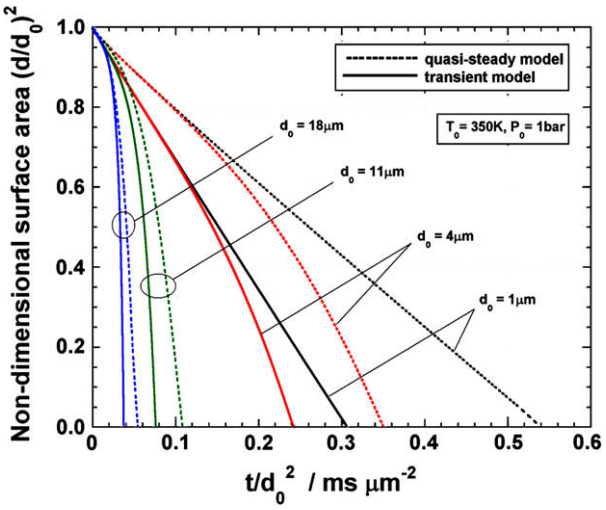

Fig. 3. Non-dimensional droplet surface areas as a function of normalized time for various sized droplets at an initial temperature and pressure of 350 K and 1 bar, respectively. Differences in predictions for the QS and TS evaporation models are visible, as are the effects of gas-phase compression on the evaporation process.

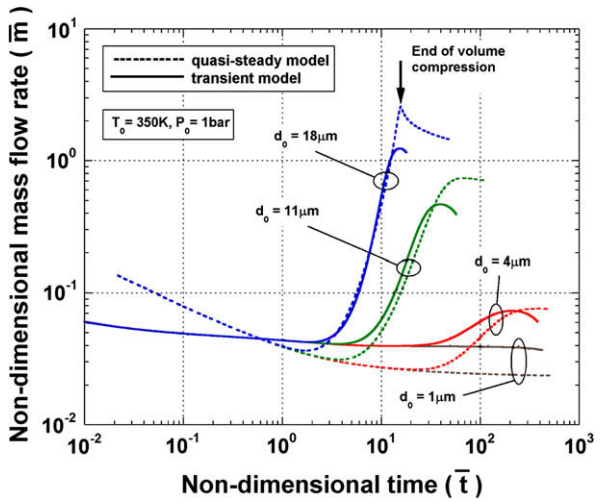

Fig. 4. Non-dimensional evaporation rates as a function of non-dimensional time for a range of initial droplet sizes. Initial temperature and pressure are 350 K and 1 bar, respectively. Differences in predictions for the QS and TS evaporation models are visible, as are the effects of gas-phase compression on the evaporation process.

is discussed more in reference to the Figs. 3–7. Additionally beneficial is the rise in the density-weighted mass diffusivity (i.e., $\rho_g D_{gk}$) which increases $\propto T^{0.75}$ due to the compression heating; the heat diffusivity κ_g however decreases $\propto T^{-1.85}$ which is not beneficial. Also shown in Fig. 2 are the effects that two of the modifications to the QS model have on the computed evaporation process. These changes, which were mentioned in Section 3, include (i) accounting for the variations in droplet thermo-physical properties with temperature (i.e., the $d\hat{\rho}_l/dt$ term in Eq. (A7)), and (ii) modifying the computational grid during the gas-phase compression step. To illustrate the effect of the second change the simulation was conducted by employing Eqs. (A11) and (A12), but without any remeshing of the computational grid. These two modifications both result in decreases in evaporation times on the order of 8% each for the 18 μm droplet. Finally, in this figure it can be seen that for all of the cases the QS model predicts slower evaporation times relative to the TS model; this finding is consistent with previous

Author's personal copy

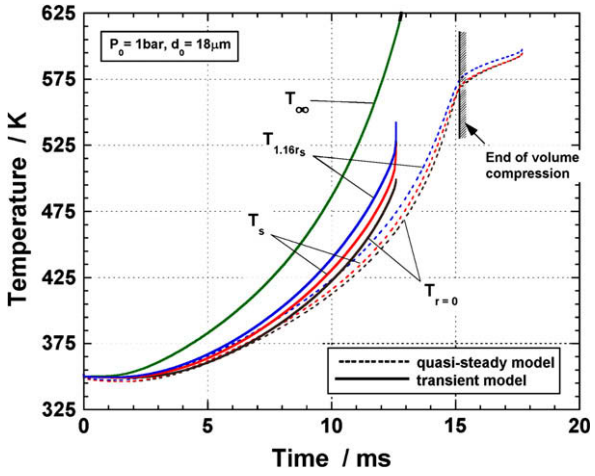

Fig. 5. Liquid- and gas-phase temperatures as a function of time at different spatial locations for a droplet with $d_0 = 18$ μm, and initial temperature and pressure of 350 K and 1 bar, respectively. Differences in predictions for the QS and TS evaporation models are visible; the T_∞ trajectory is identical for both models.

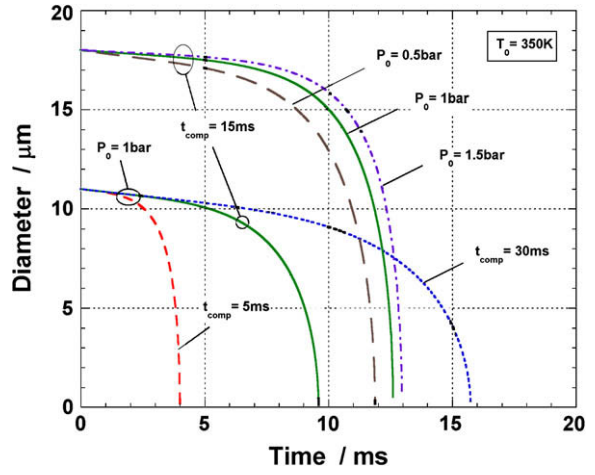

Fig. 6. Droplet diameters as a function of time for droplets with $d_0 = 18$ μm and $d_0 = 11$ μm illustrating effects of various initial pressures ($P_0 = 0.5$, 1.0 and 1.5 bar) and rates of compression ($t_{comp} = 5$, 15, 30 ms), respectively. An initial temperature of 350 K is used for all six cases.

studies where these two models have been used in simulations with an invariant background gas, e.g., see Ref. [28]. The differences between the QS and TS models are explored more in Figs. 3–5.

In Fig. 3 non-dimensional surface areas, $(d/d_0)^2$, are plotted as a function of normalized time, t/d_0^2, for the four $T_0 = 350$ K, $P_0 = 1$ bar cases shown in Fig. 2; the QS and TS results are both shown. It can be seen that the trajectories for the smallest droplet is nearly linear during evaporation for both QS and TS models, consistent with d^2-law behavior. There is a slight curvature seen here, a positive concavity, where this is a function of the initial droplet *cooling* caused by evaporation. This behavior is due to the initial conditions used in these simulations where the gas-phase is assumed to have the same temperature as the droplet, but it is initialized as only containing nitrogen. It should be noted that this behavior is different from typical droplet evaporation studies where droplets are usually *heated* during their initial exposure to a higher temperature surrounding gas; the non-dimensional surface area therefore increases as a result. In Fig. 3 it can also be seen that for droplets of greater initial diameter the departure from d^2-law behavior is

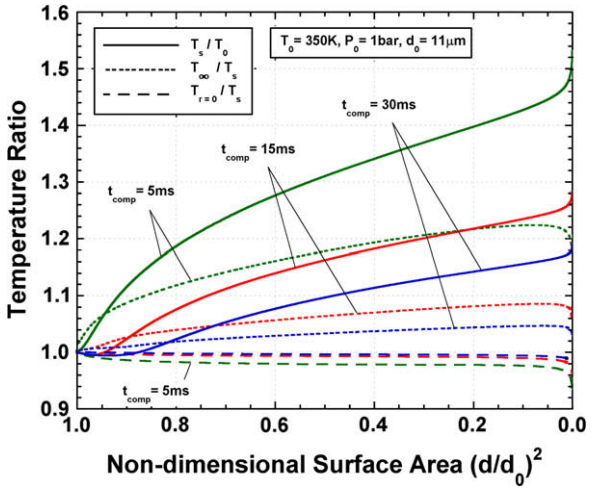

Fig. 7. Ratios of surface temperature to initial temperature, far-field temperature to surface temperature, and interior temperature to surface temperature as a function of non-dimensional droplet area for three compression times. Initial temperature and pressure of 350 K and 1 bar, respectively, are used and the initial diameter is $d_0 = 11$ μm.

more significant. This is due to two effects. One is the substantial increase in the droplet temperature and corresponding saturation pressure (fugacity) that results from the increasingly significant gas-phase compression that the droplet experiences. The other is the unsteady gas-phase boundary condition caused by gas-phase volumetric compression.

The effects of gas-phase compression heating on the evaporation rates and droplet temperatures are illustrated in Figs. 4 and 5. In Fig. 4 the non-dimensional mass flow rate, defined as $\dot{m}/4\pi\rho_g D_g r_s$, is plotted as a function of non-dimensional time, which is defined as $\int \hat{\kappa}_l dt/r_s^2$, for the four cases shown in Fig. 3. Again, results for both QS and TS models are displayed. For all of the conditions and for both models the initial *decrease* in evaporation rates due to evaporative cooling is evident. After the initial drop in temperature the evaporation rate for the smallest droplet ($d_0 = 1$ μm) remains fairly constant, which is consistent with Figs. 2 and 3. The other droplets however experience an increase in their evaporation rates, to varying degrees, depending upon the rise in liquid-phase temperature for each. The $d_0 = 18$ μm droplet sees the largest increase in temperature during its lifetime because it takes the longest to evaporate and this is reflected in its more significant increase in surface flow rate. Also visible in this figure is that the QS model initially predicts a *faster* evaporation rate relative to the TS model; this results in a more significant reduction in droplet temperature. This feature is one contributing reason for the extended evaporation times seen with the QS model in this study. A second cause is discussed next with regard to Fig. 5.

In Fig. 5 select temperatures within the computational domain are illustrated as a function of time for droplets where $d_0 = 18$ μm, $T_0 = 350$ K and $P_0 = 1$ bar; results for both the QS and TS models are shown. Temperatures at the droplet surface, the droplet center, the far-field, and at a location in the gas-phase near the near the droplet surface, i.e., $r = 1.16r_s$, are included. The initial decrease in droplet temperature and corresponding near-droplet gas-phase temperature due to evaporative cooling are visible, especially for the QS model. Also noticeable here is that there is little thermal stratification (~10 K) within the droplet (for both models), where this droplet size is the largest explored in this study. This result indicates that it may be possible to use a simplified liquid-phase model under the conditions of interest for this study. Lastly, it can be seen that after the droplet and near-droplet temperatures begin to rise, both the gas- and liquid-phase temperatures for the

Author's personal copy

TS model rise more rapidly compared to the QS model. This more rapid rise in temperature, in this case due to gas-phase transients that are not included in the QS model, results in a higher relative saturation pressure (fugacity) and thus a more rapid rate of evaporation in the TS model. To segregate the effects of gas-phase transients from the effect of initial evaporative cooling, additional simulations were conducted (not presented here) where the gas-phase computational domain was initialized as containing both nitrogen and *n*-dodecane (at the saturated condition), thereby eliminating the initial evaporative cooling process. For this modified initial condition the temperature rise rates for the TS model were also more rapid than the QS model confirming the effects of gas-phase transients on the evaporation predictions.

Figs. 6 and 7 next illustrate results investigating the influence of initial pressure and of piston compression time on the evaporation process; in these figures only results for the TS model are presented. For the variation in initial pressure, conditions of $P_0 = 0.5$, 1.0 and 1.5 bar are used, with $T_0 = 350$ K and $d_0 = 18$ μm. The peak compressed pressures for the three cases are 13.9, 27.8 and 41 bar, respectively. The 18 μm droplet is used for these simulations in order to explore possible effects of non-ideal gas behavior at the higher pressures, where this has the potential to alter the fugacity term in Eq. (B11) (i.e., ϕ_k^g) as well as the density-weighted mass diffusivities in Eqs. (B2) and (B4) (i.e., $\rho_g D_{gk}$), and the thermal diffusivity in Eq. (B4) (i.e., $\kappa_g = \alpha_g/\rho_g c_{pg}$) especially near the droplet. Throughout the droplets' lifetimes however, z_s remains close to 1.0 so that real gas effects are essentially non-existent. The difference in evaporation times seen in Fig. 6 between these three cases is thus dominated by the difference in relative fuel concentration near the droplet surface, with higher concentrations present at the lower ambient pressures. For the highest initial pressure however, i.e., $P_0 = 1.5$ bar, the droplet experiences a more significant increase in temperature resulting from gas-phase compression, and therefore the rate of liquid consumption near the end of evaporation is noticeably quicker. This result confirms, as with the Liu et al. study [39], that there is an opposing effect of pressure as temperature and pressure are simultaneously increased due to volumetric compression. However, the latter effect dominates for the conditions investigated here, a result somewhat different from that reported in Ref. [39].

For the investigation of compression time effects, three conditions are explored including t_{comp}=5, 15 and 30 ms, where the initial temperature and pressure are set to 350 K and 1 bar, respectively, and an initial droplet diameter of $d_0 = 11$ μm is used. In Fig. 6 it is clear that more rapid rates of gas-phase compression result in faster rates in overall evaporation. This is primarily due to the more rapid rise in gas- and liquid-phase temperatures (and corresponding fugacity); this is discussed next with regard to Fig. 7 which presents three temperature ratios plotted as a function of non-dimensional droplet surface area for the three cases shown in Fig. 6. The ratios include the surface temperature to initial temperature, the far-field temperature to surface temperature, and the droplet's center temperature to surface temperature. The T_s/T_0 ratio indicates how significantly the droplet surface temperature, and thus fugacity change during the wet compression process. The fastest compression time results in the most significant rise in droplet temperature, while the slowest compression time allows a greater fraction of the liquid to evaporate before the temperature increases. The total temperature rise for the $t_{comp} = 30$ ms case is much lower than the $t_{comp} = 5$ ms case. The T_∞/T_s ratio indicates the extent of far-field temperature rise relative to the conditions near the droplet. For the $t_{comp} = 5$ ms case significant stratification near the droplet within the gas phase develops since there is not adequate time for heat to diffuse to (and mass from) the droplet during the compression process. For the $t_{comp} = 30$ ms case however, the stratification is less significant with more uniform conditions seen across the gas-phase. The $T_{r=0}/T_s$ ratio provides an indication of the extent of thermal stratification within the droplet. For the two slowest compression times the $d_0 = 11$ μm droplet has a fairly uniform temperature distribution; however, just as with the gas-phase, the fastest compression condition leads to more significant stratification within the droplet as there is not adequate time for heat to diffuse to the center. For RCM applications it is desirable to minimize local (and bulk) thermal and concentration stratification as this can result in non-homogeneous chemical reactions across the reaction chamber, and thus contaminated ignition data sets. Slower compression times may therefore be more favorable to achieving uniform conditions.

Finally, Fig. 8 is presented to summarize the parametric results of this study where the TS model is used covering $T_0 = 300$–380 K, $d_0 = 1$–18 μm and $p_0 = 1$ bar. The intent of this figure is to indicate regions of acceptable operation for an RCM utilizing wet compression with *n*-dodecane as the fuel. In order for a wet compression RCM experiment to be successful the liquid must completely vaporize and diffuse throughout surrounding gas (i.e., the oxidizer/diluent) before the gas-phase achieves conditions that are favorable for chemical reaction. For *n*-dodecane and fuels with similar low temperature reactivity, the target completion temperature is 500 K; after this point significant fuel decomposition could occur on time scales similar to the evaporation process [42]. Indicated in this figure is an upper bound for droplet diameters based on their initial temperatures which are predicted to evaporate before $T_\infty = 500$ K. Also shown are evaporation trajectories for two individual droplets ($T_0 = 350$ K, $d_0 = 4$ μm and 11 μm) including both the surface and far-field temperatures. The extent of thermal (and by analogy compositional) stratification is visible, where this is more significant for the $d_0 = 11$ μm droplet. At initial pressures greater or lower than 1 bar this 'operating map' will be shifted due to reduced or increased (respectively) fuel concentrations at the droplet surface, as discussed earlier with regard to Fig. 6. Also drawn in Fig. 8 is an upper limit for the initial temperature ($T_0 \sim 375$ K) where this is estimated based on machine integrity issues as discussed in Section 1. It should be noted however, that this 'operating map' does not take into account gas-phase evaporative cooling or fuel saturation at the far-field which could be important under high fuel loading (e.g., stoichiometric) conditions and which could shift the bounds of the acceptable region. These effects are explored in a forthcoming study.

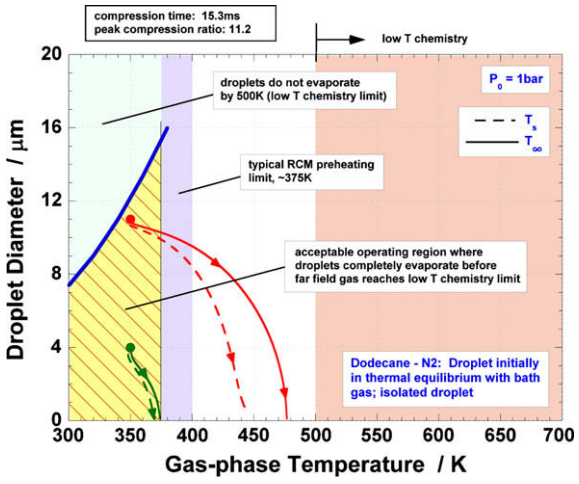

Fig. 8. Droplet diameter as a function of temperature illustrating evaporation trajectories (T_s and T_∞) for droplets with $T_0 = 350$ K, $P_0 = 1$ bar and $d_0 = 4$, 11 μm, as well as the maximum possible droplet size at a given initial temperature that will ensure complete evaporation before the far-field reaches the low temperature chemistry region. The heating limit of typical RCMs is highlighted.

Author's personal copy

5. Summary

The evaporation characteristics of a single fuel droplet subjected to gas-phase compression heating (i.e., wet compression) is investigated using two spherically-symmetric models; one employs a quasi-steady approximation while the other accounts for gas-phase transients, as well as viscous transport and pressure variations across the computational domain. Temperature and pressure dependent properties are utilized and the compression history from a typical rapid compression machine is employed to prescribe the rate of volumetric compression. *n*-Dodecane is used as the fuel with the surrounding gas assumed to be initially only nitrogen. A range of conditions is simulated with the two models in order resolve discrepancies between previous studies and to better understand the characteristics of the evaporation process.

The simulations have verified that wet compression can significantly increase the rate of evaporation with this primarily due to the increase in droplet temperature and corresponding saturation pressure (fugacity). The increase in the density-weighted mass diffusivity is also beneficial in reducing the droplet consumption times, while the reduction in gas-phase heat diffusivity has an opposing effect. The QS model is found to predict substantially longer rates of evaporation relative to the TS model. These differences can be attributed to the fact that the time scales associated with wet compression are of the same order of magnitude as those associated with liquid-phase processes, and this results in two effects. First, the initial rates of evaporation for the QS model are faster and this leads to more evaporative cooling of the droplet which reduces the saturation pressure (fugacity). Second, the gas-phase transients associated with the compression process result in higher temperatures near the droplet in the TS model and this leads to faster overall consumption times. Pressure effects under the conditions explored here (i.e., $z_s \sim 1$), are primarily associated with changes to the fuel concentration at the droplet surface such that the larger pressures result in longer consumption times. The effects of simultaneous pressure and temperature increase for the conditions investigated here are dominated by temperature effects. The TS model predicts negligible pressure variations across the computational domain for all of the conditions explored in this study.

Finally, increasing rates of volumetric compression can lead to faster evaporation times, however there is a corresponding increase in spatial stratification, in both the gas and liquid phases, and this many not be advantageous for RCM applications. An 'operating map' has been estimated for a single *n*-dodecane fuel droplet evaporating into nitrogen at an initial pressure of 1 bar. This map does not take into account far-field evaporative cooling or fuel saturation that would be experienced in high fuel loading conditions; however, it does provides an indication that droplets smaller than those used in Refs. [16,17] may be required for successful RCM operation with fuels having significant low temperature reactivity. Effects of evaporative cooling and fuel saturation are important, as are thermo-physical properties such as fugacity and mass diffusivity for other low vapor pressure fuels and these will be investigated in a forthcoming study.

Acknowledgements

Professor Rolf Reitz at the University of Wisconsin Engine Research Center is thanked for his assistance in locating a copy of the original source code for the TS model. Many useful suggestions by the reviewers are acknowledged. Funding for this work has been provided in part through NSF CBET-0521602 and Marquette University's Committee on Research. The parametric simulations were conducted using the Open Computing system at LLNL and Marquette University's Cluster Computing Center.

Appendix A. Quasi-steady evaporation model

This appendix summarizes the quasi-steady (QS) evaporation model used in this study. The model is based on work by Aggarwal and co-workers [21,22,24] and utilizes a continuum formulation for a spherically symmetric droplet. Modifications to the model for this study include accounting of the time-varying (temperature-dependent) properties of the liquid-phase, and incorporating a method to simulate compression heating of the gas-phase. Uniform pressure is assumed across the computational domain and phase equilibrium is prescribed at the droplet surface; the surrounding gas is not absorbed into the droplet. The gas-phase, liquid-phase and compression heating components of the model are presented next.

A.1. Quasi-steady gas-phase model

A single isolated fuel droplet is assumed to evaporate in an environment where the temperature and pressure are dynamically elevated due to piston compression. The gas-phase transport processes are considered to be quasi-steady, which implies that the characteristic gas-phase time is much shorter compared to the liquid-phase transient time, including the time associated with the surface regression. This formally requires that the ratio of gas density to liquid density be at least an order of magnitude smaller than unity (i.e., $\rho_g/\rho_l < 0.1$). Other assumptions include spherical symmetry, phase-equilibrium at the droplet surface, and negligible secondary diffusion and radiation. Using these approximations the energy and fuel-vapor species conservation equations can be simplified to a steady, one-dimensional form, as shown in Ref. [19]

$$\frac{d}{dr}\left(r^2\rho_g u c_{pg}(T_g - T_s) - r^2\rho_g D_g c_{pg} Le_g \frac{d(T_g - T_s)}{dr}\right) = 0 \tag{A1}$$

$$\frac{d}{dr}\left(r^2\rho_g u Y_f - r^2\rho_g D_g \frac{dY_f}{dr}\right) = 0 \tag{A2}$$

Here r is the radial coordinate, u is the gas or Stefan flow velocity, Le_g is the gas-phase Lewis number (κ_g/D_g), and Y_f is the mass fraction of fuel vapor. In addition, T_g is the ambient temperature, T_s is the droplet surface temperature, ρ_g is the gas-phase density, c_{pg} is the gas-phase specific heat at constant pressure and D_g is the gas-phase binary diffusion coefficient (for fuel into ambient gases). With the boundary conditions such that $T_g = T_\infty$ and $Y_f = Y_{f\infty}$ at $r = r_\infty$ the solution to these equations is

$$\frac{\dot{m}}{4\pi\rho_g D_g Le_g}\left[\frac{1}{r_s} - \frac{1}{r_\infty}\right] = \ln\left[1 + \frac{c_{pg}(T_\infty - T_s)}{H}\right] \tag{A3}$$

$$\frac{\dot{m}}{4\pi\rho_g D_g}\left[\frac{1}{r_s} - \frac{1}{r_\infty}\right] = \ln\left[\frac{1 - Y_{f\infty}}{1 - Y_{fs}}\right] \tag{A4}$$

Here r_s and r_∞ represent the radial locations at the droplet surface and far away from the droplet, respectively, and H is the energy supplied to the droplet per unit mass of fuel vaporized, in order to heat the droplet and to vaporize the fuel. Using this formulation the natural log term in Eq. (A4) can be written as

$$\frac{1 - Y_{f\infty}}{1 - Y_{fs}} = 1 + B \tag{A5}$$

where B is referred to as the mass transfer number [19]. Combining Eqs. (A3), (A4), and (A5) an expression for H can be derived such that

Author's personal copy

$$H = \frac{c_{pg}(T_s - T_\infty)}{1-(1+B)^{-Le_g}} \tag{A6}$$

With this formulation the rate of surface regression can be determined by

$$\frac{dr_s^2}{dt} = -\frac{\dot{m}}{2\pi r_s \hat{\rho}_l} + \frac{2r_s^2}{3\hat{\rho}_l}\frac{d\hat{\rho}_l}{dt} \tag{A7}$$

where $\hat{\rho}_l$ is the volume-averaged liquid-phase density. The second term on the right-hand side of this expression accounts for changes in the liquid-phase density due to the compression heating process. This contribution is found to be significant for droplets that experience large changes in temperature during wet compression with differences in evaporation times on the order of ~5–10% (e.g., see Fig. 2).

A.2. Liquid-phase diffusion-limit model

The heat and mass transport inside the droplet are assumed to be governed by the transient heat and mass diffusion equations. These equations involve a moving boundary and because of this a transformation is used to cast the moving boundary (i.e., the droplet surface) into a fixed one. The transformed equations can be expressed as (e.g., see Ref. [19]),

$$\begin{aligned}\frac{\partial \bar{T}_l}{\partial \bar{t}} &= \frac{1}{\hat{\kappa}_l \rho_l c_{pl} \bar{r}^2}\frac{\partial}{\partial \bar{r}}\left(\alpha_l \bar{r}^2 \frac{\partial \bar{T}_l}{\partial \bar{r}}\right) - \bar{r}\,\bar{m}\frac{\rho_g D_g}{\hat{\rho}_l \hat{\kappa}_l}\frac{\partial \bar{T}_l}{\partial \bar{r}} \\ &\quad - \bar{T}_l\left(\frac{1}{\rho_l}\frac{\partial \rho_l}{\partial \bar{t}} + \frac{1}{c_p l}\frac{\partial c_{pl}}{\partial \bar{t}}\right) \\ &\quad - \bar{T}_l\left\{\bar{r}\,\bar{m}\frac{\rho_g D_g}{\hat{\rho}_l \hat{\kappa}_l} - \frac{\bar{r}}{3\hat{\kappa}_l}\frac{r_s^2}{\hat{\rho}_l}\frac{\partial \hat{\rho}_l}{\partial t}\right\}\left(\frac{1}{\rho_l}\frac{\partial \rho_l}{\partial \bar{r}} + \frac{1}{c_{pl}}\frac{\partial c_{pl}}{\partial \bar{r}}\right) \\ &\quad + \frac{\bar{r}}{3\hat{\kappa}_l}\frac{r_s^2}{\hat{\rho}_l}\frac{\partial \hat{\rho}_l}{\partial t}\frac{\partial \bar{T}_l}{\partial \bar{r}}\end{aligned} \tag{A8}$$

where the first two terms on the right-hand side represent the traditional, constant-property formulation, while the other three account for changes in the liquid-phase properties due to droplet heating. The temperature and thus property changes are large for some of the cases considered here; however, the effects on temperature distribution within the droplets are found to be small, so that these terms could be neglected for the conditions explored here.

The initial and boundary conditions for Eq. (A8) are

$$\begin{aligned}&\bar{T}_l = 0 \quad \text{at } \bar{t} = 0 \\ &\frac{\partial \bar{T}_l}{\partial \bar{r}} =; 0 \quad \text{at } \bar{r} = 0 \\ &\frac{\partial \bar{T}_l}{\partial \bar{r}} = \bar{m}\frac{\rho_g D_g}{\kappa_{l,s} T_{ref}}(H - L) \quad \text{at } \bar{r} = 1\end{aligned} \tag{A9}$$

where $\bar{T}_l(\bar{r},\bar{t})$, $\bar{r}$, $\bar{t}$, and $\bar{m}$ are the normalized liquid-phase temperature, radial location, temporal variable, and vaporization rate, respectively. These normalized variables are given by

$$\begin{aligned}&\bar{T}_l = \frac{T_l}{T_{ref}} \\ &\bar{r} = r/r_s \\ &\bar{t} = \int_0^t \frac{\hat{\kappa}_l}{r_s^2}dt \\ &\bar{m} = \frac{\dot{m}}{4\pi\rho_g D_g r_s}\end{aligned} \tag{A10}$$

with T_{ref} representing a reference temperature, r_s the instantaneous droplet radius, and $\hat{\kappa}_l$ the volume-average liquid-phase thermal diffusivity. In addition, α_l is the liquid-phase thermal conductivity, c_{pl} is the liquid-phase specific heat at constant pressure, and L is the heat of vaporization. A Crank–Nicolson implicit scheme with a variable grid spacing is employed to solve the set of equations.

A.3. Gas-phase compression heating

The gas-phase compression process is implemented using an operator splitting technique where this is simulated by physically compressing the gas-phase computational mesh at each time step, thereby increasing the density of the individual computational cells and the associated internal energy (i.e., temperature). This approach accounts for the convective flow that occurs towards the droplet as a result of wet compression. Using this methodology the volumetric compression can be expressed as

$$\rho_{g,ii}^{n+1} = \rho_{g,ii}^{n}(V^n/V^{n+1}) \tag{A11}$$

where n and n+1 represent the nth and n+1 time steps, and V is the volume of a reaction chamber, such as the combustion chamber in an IC engine, or the internal volume of an RCM. The gas-phase compression is assumed to occur adiabatically (and reversibly) and thus the compressed pressure can be expressed as,

$$P^{n+1} = P^n(V^n/V^{n+1})^\gamma \tag{A12}$$

where γ is the isentropic expansion coefficient, which reduces to the ratio of gas-phase specific heats, i.e., c_{pg}/c_{vg}, for ideal gas conditions. P is pressure in this expression. The specific heat ratio is computed using molar-weighted properties averaged over the gas-phase domain. The new cell temperatures are determined using the ideal gas equation of state.

A.4. Solution procedure

The solution procedure for the quasi-steady model involves first a calculation of the phase-equilibrium at the droplet surface with the surface temperature, T_s, used from the previous time step. The average gas-phase temperature and species mass fractions are then computed using Eq. (A11) and the thermo-physical and transport properties of the gaseous mixture calculated with expressions described previously. The volume-averaged liquid fuel properties including specific heat, thermal conductivity, and density are then computed. The new T_s is next determined using the diffusion-limit model discussed in Section A.2 and the droplet radius is calculated from Eq. (A6). Finally, the compressed densities and pressure of the gas-phase are computed using Eqs. (A11) and (A12).

Appendix B. Transient evaporation model

This appendix summarizes the transient evaporation model used in this study. The model is based on work by Aggarwal and co-workers [26–29] and utilizes a continuum formulation for a spherically symmetric droplet. Modifications to the model for this study are primarily to account for the compression heating of the gas-phase, and to incorporate some thermo-physical models that are consistent with the quasi-steady evaporation model.

The transient two-phase governing equations are written in a spherical coordinate system with phase equilibrium prescribed at the droplet surface. Radiation and second-order effects, such as the Soret and Dufour effects, are assumed to be negligible. The model considers mass, species, momentum and energy conservation throughout the gas-phase domain and it considers absorption of gas into the liquid phase, while resolving species diffusion process within the droplet. Both the gas- and liquid-phase properties are considered to be functions of species, temperature and pressure, and an adaptive grid is used to account for the surface regression. An operator splitting technique is incorporated to physically compress the computational mesh at each time step to account for compression heating of the gas-phase. The governing equations and the inter-phase conditions at the droplet surface are reviewed next.

Author's personal copy

B.1. Governing equations

For the gas-phase region $r > r_s(t)$, the governing equations include the conservation equations for mass, species, momentum, energy and the equation of state (EOS):

$$\frac{\partial \rho_g}{\partial t} + \frac{1}{r^2}\frac{\partial}{\partial r}(\rho_g u r^2) = 0 \tag{B1}$$

$$\frac{\partial \rho_{gk}}{\partial t} + \frac{1}{r^2}\frac{\partial}{\partial r}(\rho_{gk} u r^2) = \frac{1}{r^2}\frac{\partial}{\partial r}\left[\rho_g D_{gk} r^2 \frac{\partial Y_k}{\partial r}\right] \tag{B2}$$

$$\frac{\partial \rho_g u}{\partial t} + \frac{1}{r^2}\frac{\partial}{\partial r}(\rho_g u^2 r^2) + \frac{\partial P}{\partial r} = \frac{1}{r^2}\frac{\partial}{\partial r}\left[2\mu_g r^2 \frac{\partial u}{\partial r} + \lambda_g \frac{\partial}{\partial r}(ur^2)\right] - \frac{2}{r^2}\left[2\mu_g u + \frac{\lambda_g}{r}\frac{\partial}{\partial r}(ur^2)\right] \tag{B3}$$

$$\begin{aligned}\frac{\partial \rho_g I}{\partial t} &+ \frac{1}{r^2}\frac{\partial}{\partial r}(\rho_g I u r^2) + \frac{P}{r^2}\frac{\partial}{\partial r}(ur^2) \\ &= \frac{1}{r^2}\left\{\frac{\partial}{\partial r} r^2 \rho_g \left[\sum_{k=1}^{N} D_{gk} h_{gk} \frac{\partial Y_k}{\partial r}\right]\right\} + \frac{1}{r^2}\frac{\partial}{\partial r}\left(\alpha_g r^2 \frac{\partial T_g}{\partial r}\right) \\ &\quad + \frac{\partial u}{\partial r}\left[2\mu_g \frac{\partial u}{\partial r} + \frac{\lambda_g}{r^2}\frac{\partial}{\partial r}(ur^2)\right] + \frac{2u}{r^2}\left[2\mu_g u + \frac{\lambda_g}{r}\frac{\partial}{\partial r}(ur^2)\right]\end{aligned} \tag{B4}$$

$$f_1(T_g, P, \rho_{g1}, \rho_{g2}, \ldots, \rho_{gN}) = 0 \tag{B5}$$

In Eqs. (B1), (B2), (B3), (B4), (B5), t and r refer to temporal and spatial variables, respectively, and ρ_{gk}, D_{gk}, Y_k, and h_{gk} represent the gas-phase density, diffusion coefficient, mass fraction and specific enthalpy of the kth species, respectively, with N the total number of species. The parameters α_g, μ_g, and λ_g are the gas-phase thermal conductivity, viscosity, and second viscosity coefficient, respectively. In addition, u is velocity, T_g temperature, P pressure and I mass-specific internal energy. Eq. (B5) is a P–ρ–T relation for the fluid mixture, such as the ideal gas or Peng–Robinson EOS.

For the liquid-phase region, $r < r_s(t)$, the governing equations include only species and energy diffusion

$$\frac{\partial \rho_{lk}}{\partial t} = \frac{1}{r^2}\frac{\partial}{\partial r}\left[\rho_{lk} D_{lk} r^2 \frac{\partial X_k}{\partial r}\right] \tag{B6}$$

$$\frac{\partial}{\partial t}(\rho_l c_{pl} T_l) = \frac{1}{r^2}\frac{\partial}{\partial r}\left(\alpha_l r^2 \frac{\partial T_l}{\partial r}\right) + \frac{1}{r^2}\left\{\frac{\partial}{\partial r} r^2 \left[\sum_{k=1}^{N} \rho_l D_{lk} h_{lk} \frac{\partial X_k}{\partial r}\right]\right\} \tag{B7}$$

In these expressions the subscript 'l' denotes the liquid phase, and c_p is the specific heat at constant pressure; X_k is the mass fraction of species k in the liquid-phase.

B.2. Boundary conditions

The boundary conditions at the droplet center ($r = 0$) are: $\partial T_l / \partial r = 0$ and $\partial \rho_k / \partial r = 0$; for the far-field the standard boundary conditions are applied: $T_g \to T_\infty$, $P \to P_\infty$, $\rho_{gk} \to \rho_{k\infty}$. On the droplet surface, $r = r_s(t)$, the conditions of mass and energy conservation, and of thermodynamic equilibrium can be expressed as

$$\dot{m} X_k - \rho_{lk} D_{lk} \left.\frac{\partial X_k}{\partial r}\right|_{r=r_s^-} = \dot{m} Y_k - \rho_{gk} D_{gk} \left.\frac{\partial Y_k}{\partial r}\right|_{r=r_s^+} \tag{B8}$$

$$\begin{aligned}-\alpha_l \left.\frac{\partial T_l}{\partial r}\right|_{r=r_s^-} &= -\alpha_g \left.\frac{\partial T_g}{\partial r}\right|_{r=r_s^+} + \sum_{k=1}^{N}\left(\dot{m} Y_k - \rho_{gk} D_{gk} \frac{\partial Y_k}{\partial r}\right)\Bigg|_{r=r_s^+} L_k \\ &\quad + \dot{m}\left[\frac{u^2}{2} - u\frac{dr_s}{dt} - \frac{2\mu_g}{\rho}\frac{\partial u}{\partial r} + \frac{\lambda_g}{r^2}\frac{\partial}{\partial r}(ur^2)\right]\end{aligned} \tag{B9}$$

$$f_2(T_s, P_s, X_{1s}, X_{2s} \ldots X_{Ns}, Y_{1s}, Y_{2s} \ldots Y_{Ns}) = 0 \tag{B10}$$

where $\dot{m}$ is the droplet vaporization rate, and X_{ks} and Y_{ks} represent respectively, the liquid- and gas-phase mole fractions of the kth species at the droplet surface. The latent heat of vaporization of species k is L_k. The specific form of Eq. (B10) can be derived from the condition of thermodynamic and mechanical equilibrium at the droplet surface presented in the next section.

In supercritical environments (not seen for the conditions explored here) the droplet may experience a thermodynamic state transition from sub-critical to supercritical. Eqs. (B8), (B9), and (B10) are only applicable until the droplet surface reaches a critical mixing point; at the critical mixing point, the droplet surface becomes indistinguishable from the gas-phase. The subsequent droplet regression is then characterized by the motion of the critical surface which moves inward continuously, as discussed extensively in Refs. [18,19]. These effects are taken into account in the evaporation software.

B.3. Vapor–liquid equilibrium at the droplet surface

When the droplet surface is in mechanical and thermodynamic equilibrium, the temperature, pressure and fugacity of each species in the gas phase is equal to the corresponding property of the same species in the liquid phase. The equality of the fugacity of species k is expressed as

$$\phi_k^g Y_k = \phi_k^l X_k \tag{B11}$$

where ϕ_k is the fugacity coefficient of the kth species, and is a function of pressure, temperature and composition. It is given generally in terms of the volumetric properties of the mixture by the following thermodynamic relation:

$$RT \ln(\phi_k) = \int_{\upsilon}^{\infty}\left[\left(\frac{\partial P}{\partial n_k}\right)_{T,\upsilon,n_j} - \frac{RT}{\upsilon}\right] d\upsilon - RT \ln z \tag{B12}$$

where n_j is the mole number of the jth species and z is the compressibility factor, $z = P\upsilon/RT$. Eqs. (B11) and (B12) provide the basic relations for vapor–liquid equilibrium calculation. These expressions, along with Eqs. (B8) and (B9), provide a closed system to determine the temperature and species mole fractions at the droplet surface. These represent a system of highly non-linear algebraic equations that are solved iteratively at each time step.

For systems with multi-component mixtures the latent heat of vaporization of each species is defined as the difference between the partial molar enthalpy of that species in the vapor and liquid phases. The following thermodynamic relation then gives the partial molar enthalpy of the k^{th} species:

$$L_k = h_{lk} - h_k^0 = -RT^2 \frac{\partial}{\partial T} \ln \phi_k \tag{B13}$$

where the superscript '0' denotes the property in the ideal gas state. This equation is solved iteratively along with Eqs. (B8), (B9) and (B11), (B12).

B.4. Gas-phase compression heating

The gas-phase compression process is computed similarly as with the quasi-steady model where the computational mesh is physically compressed at each time step thereby increasing the density of the computational cells (Eq. (A11)) and the associated internal energy. The gas-phase compression is assumed to occur adiabatically so that the new cell specific internal energy can be determined based on energy conservation

$$I_{ii}^{n+1} = I_{ii}^{n} - \int_{\upsilon_{ii}^{n}}^{\upsilon_{ii}^{n+1}} P_{ii} d\upsilon \tag{B14}$$

Author's personal copy

The PR-EOS (Eqs. (B6)–(B10)) is used in conjunction with these expressions to iteratively determine the resulting cell pressure and temperature. Momentum of each gas-phase computational cell is also conserved during the compression operation, where this is expressed as

$$(\rho_g u)_{ii}^{n+1} = (\rho_g u)_{ii}^{n} \tag{B15}$$

B.5. Solution procedure

An arbitrary Lagrangian–Eulerian numerical method with a dynamically adaptive mesh is used to solve the governing equations. The solution procedure, as discussed in Ref. [28] is as follows: (i) calculate explicitly the contributions of the diffusion and source terms in the gas-phase equations, (ii) calculate implicitly the terms associated with the acoustic pressure in the gas-phase equations; (iii) compute a new mesh distribution due to droplet surface regression using the adaptive mesh method, and then the convective terms in the gas-phase equations, (iv) based on the solutions of the above steps, solve implicitly the gas-phase equations, along with the liquid phase equations and the droplet surface and liquid-vapor equilibrium equations, and (v) perform the gas-phase compression step.

An algorithm is employed in this study to adaptively resize the gas-phase computational cells based on the magnitude of temperature gradients across the domain; higher grid densities are used near the droplet surface where higher gradients exist. A variable time step is also utilized where this is automatically adjusted depending on stability criteria of the explicit convection and diffusion processes.

Appendix C. Thermo-physical models

C.1. Quasi-steady evaporation model

The gas- and liquid-phase thermodynamic and transport properties in the quasi-steady evaporation model are considered to be primarily functions of temperature and composition. Pressure effects are included in the calculation of gas-phase diffusivity, e.g., $D_g \propto P^{-1}T_g^{1.75}$. The ideal gas equation of state is used for the gas-phase where the density is computed via $\rho_g = P/RT_g$; the density of the liquid-phase is computed based on a fourth-order polynomial fit of experimental data [45]. The heat capacity of the gas-phase is determined using a molar weighted summation of component specific heats with these computed using fifth-order polynomial fits of CHEMKIN data, derived from calculations using THERM [46]. The liquid-phase heat capacity is computed based on the group contribution model described via Rùzicka and Domalski [47]. The thermal conductivity of the gas-phase is based on a simple molar weighting with the species specific values where these are estimated based on the group contribution model presented by Roy and Thodos [48,49]. Third-order polynomial fits of the computed α_i values are used in the simulations to improve computational efficiency. The thermal conductivity of the liquid-phase fuel is determined based on the estimation method of Latini et al. [50]. The gas-phase fuel diffusivity is computed using Fuller et al.'s atomic diffusion volume empirical model [50]. The vapor–liquid equilibria at the droplet surface is approximated by Raoult's law, i.e., $X_f P = P_f^{sat}(T_s)$. The saturation pressure and the heat of vaporization, L are determined using a three-parameter corresponding states model with correlations developed by Lee and Kessler [51] and Poling et al. [50], respectively.

The mean gas-phase mixture properties are computed using the common "one-third rule" [52] where the properties are evaluated at the droplet surface and at the far-field conditions, and then weighted according to

$$F_{mean} = \frac{1}{3}F_{g,s} + \frac{2}{3}F_{g,\infty} \tag{C1}$$

In this expression F represents an arbitrary property (e.g., c_p) and the subscripts denote the surface conditions, s, and the far-field conditions, ∞. This approach enables the model to better capture the physics near the droplet surface which govern the rate of evaporation, as opposed to a volumetric averaging which would be weighted more significantly to the far-field conditions, especially for large computational domains, i.e., $r_\infty \gg r_s$.

C.2. Transient evaporation model

The gas- and liquid-phase thermo-physical properties for the transient model are considered to be functions of pressure, temperature and composition. Similar low pressure models are used between this evaporation model and the quasi-steady one. The method suggested by Chung et al. [53] is employed to calculate the viscosity of the gas mixture while the thermal conductivity is based on the group contribution model of Roy and Thodos [48,50]. The binary gas-phase mass diffusivity is calculated using the empirical model of Fuller et al. [50] with corrections for pressure effects using the Takahashi correlation [54]. For multi-component mixtures, the effective diffusivity is obtained using the formula given by Bird et al. [55]. The gas density is calculated directly from the PR-EOS [56], while the saturation condition, including ϕ_k and L_k, is also computed directly from the PR-EOS (e.g., see ref. [50]).

The enthalpy of the gas mixture is based on pure component enthalpies obtained from the CHEMKIN database (computed using the THERM software [46]). A generalized thermodynamic correlation based on a three-parameter corresponding states method [57] is used to compute the enthalpy correction for high-pressure effects. The specific internal energy of the gas mixture in Eq. (B4) is given by

$$I = \sum_{k=1}^{N} Y_k h_k(T) - P\upsilon \tag{C2}$$

which relates the specific internal energy to the equation of state through the gas temperature and pressure.

The heat capacity of pure liquid components is calculated based on the group contribution model described by Rùzicka and Domalski [47] and then extended to mixtures using Filippov's rule [58]. The liquid-phase thermal conductivity and mass diffusivity are obtained using the correlations of Latini et al. [50] and Nakanishi [59], respectively. The liquid density is calculated based on a fourth-order polynomial fit of experimental data, with these recorded near 1atm, along with the high pressure correction given by Thomson et al. [60].

Under some conditions there could be differences in the simulation results between the quasi-steady and transient evaporation models due to the different EOS and thermo-physical models employed. However, for the cases explored here these effects are found to be negligible in comparison to other effects, especially gas-phase transients. A check was conducted however, where the IG-EOS was substituted into the transient evaporation model and the high pressure contributions to the properties were eliminated; the results of this check were almost identical for all conditions.

C.3. Comparison with experimental data

Fig. C1 provides a comparison of the experimental data and property models for density, heat capacity and thermal

Author's personal copy

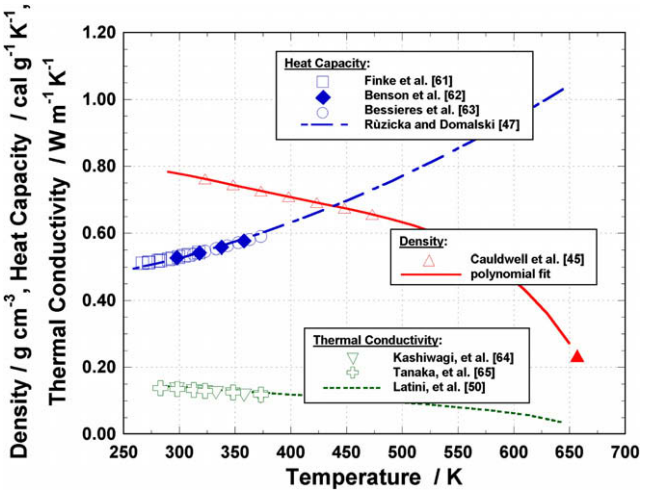

Fig. C1. Comparison of experimentally measured and model values for density, heat capacity and thermal conductivity for liquid-phase *n*-dodecane at conditions near 1 bar.

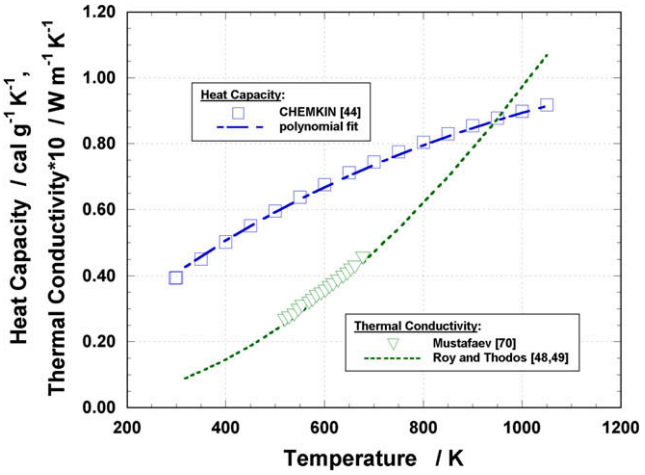

Fig. C3. Comparison of experimentally measured and model values for heat capacity and thermal conductivity for gas-phase *n*-dodecane at conditions near 1 bar.

conductivity for liquid n-dodecane. The data of Cauldwell et al. [45], Finke et al. [61], Benson et al. [62], Bessieres et al. [63], Kashiwagi et al. [64] and Tanaka et al. [65] are included. These are plotted as a function of temperature with pressures near 1atm. It can be seen that the models do an excellent job of replicating the experimental data. However, the available data covers only a narrow range of temperatures. This is due to experimental difficulties of handling n-dodecane at higher temperatures where thermally-induced decomposition can be problematic. Some of the simulated cases explored in this study indicate liquid-phase temperatures upwards of 600K and this limitation in the data should be kept in mind when reviewing the figures, e.g., Fig. 5.

In Fig. C2 the saturation pressure of n-dodecane is presented as a function of temperature. Data collected by Maia de Oliveira et al. [66], Morawaetz [67], Sasse et al. [68], and Smith et al. [69] are plotted and the normal boiling point of 488 K is highlighted. Correlations due to Lee and Kessler [51] and the Clausius–Clapyron approximation are both drawn, where the normal boiling point is chosen as the reference condition for the Clausius–Clapyron expression. It can be seen that at room temperature, which is significantly lower than the normal boiling point of *n*-dodecane, the Clausius–Clapyron approximation results in a substantial underprediction of the saturation pressure. This error results in longer computed evaporation times relative to a more accurate representation of P^{sat}. The PR-EOS saturation curve is also shown in Fig. C2 where very good agreement is seen between the Lee and Kessler correlation and the PR-EOS prediction. Vaporization enthalpies between the two models, though not shown here, also agree very well.

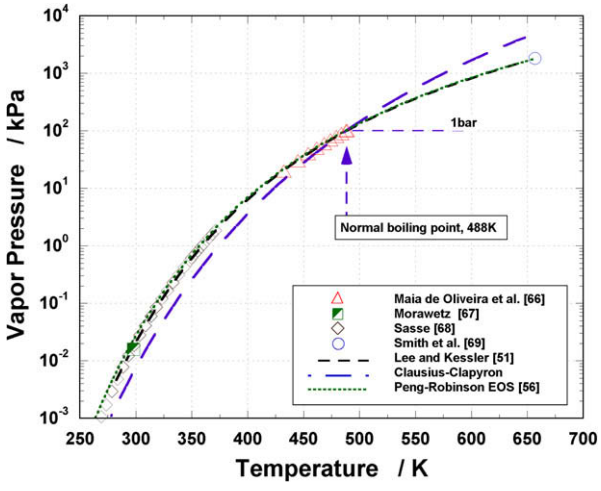

Fig. C2. Comparison of experimentally measured and model values for vapor pressure of *n*-dodecane covering conditions from near the triple point to the critical point.

The gas-phase heat capacity and thermal conductivity of *n*-dodecane are presented in Fig. C3. The CHEMKIN data [44] and the data due to Mustafaev [70] are included for reference. Excellent agreement is also seen in this figure for the c_p and α correlations used in this work. Again noticeable is the limited range of available experimental data.

References

[1] S. Kimura, O. Aoki, Y. Kitahara, E. Aiyoshizawa, Ultra-clean combustion technology combining a low-temperature and premixed combustion concept for meeting future emission standards, SAE Paper 2001-01-0200, 2001.
[2] H. Yanagihara, A study on combustion structure of premixed compression ignition diesel engines, SAE 2002-30-0009, 2002.
[3] H. Ogawa, N. Miyamoto, K. Akao, Combustion in a two-stage injection PCCI engine with higher volatility fuels, SAE 2002-08-0423, 2002.
[4] S. Simescu, S.B. Fiveland, L.G. Dodge, An experimental investigation of PCCI-DI combustion and emissions in a heavy-duty diesel engine, SAE 2003-01-0345, 2003.
[5] M. Canova, S. Midlam-Mohler, Y. Guezennec, G. Rizzoni, Theoretical and experimental investigation on diesel HCCI combustion with external mixture formation, Int. J. Vehicle Design 44 (2007) 62–83.
[6] G.C. Martin, C.J. Meuller, D.M. Milam, M.S. Radovanovic, C.R. Gehrke, Early direct-injection, low-temperature combustion of diesel fuel in an optical engine utilizing a 15-hole, dual-row, narrow-included-angle nozzle, SAE 2008-01-2400, 2008.
[7] J.H. Mack, S.M. Aceves, R.W. Dibble, Demonstrating direct use of wet ethanol in a homogeneous charge compression ignition (HCCI) engine, Energy 34 (2009) 782–787.
[8] M. Chaker, C.B. Meher-Homji, T. Mee III, Inlet fogging of gas turbine engines – part I: fog droplet thermodynamics, heat transfer, and practical considerations, J. Eng. Gas Turbines Power 126 (2004) 545–558.
[9] M. Chaker, C.B. Meher-Homji, T. Mee III, Inlet fogging of gas turbine engines – part II: fog droplet sizing analysis, nozzle types, measurement and testing, J. Eng. Gas Turbines Power 126 (2004) 559–570.
[10] M. Chaker, C.B. Meher-Homji, T. Mee III, Inlet fogging of gas turbine engines – part III: fog behavior in inlet ducts, computational fluid dynamics analysis and wind tunnel experiments, J. Eng. Gas Turbines Power 126 (2004) 571–580.
[11] R. Bhargava, C.B. Meher-Homji, Parametric analysis of existing gas turbines with inlet evaporative and overspray fogging, J. Eng. Gas Turbines Power 127 (2005) 145–158.
[12] R.K. Bhargava, C.B. Meher-Homji, M.A. Chaker, M. Bianchi, F. Melinao, A. Peretto, Gas turbine fogging technology: a state-of-the-art review – part II:

Author's personal copy

overspray fogging – analytical and experimental aspects, J. Eng. Gas Turbines Power 129 (2007) 454–460.
[13] R.K. Bhargava, C.B. Meher-Homji, M.A. Chaker, M. Bianchi, F. Melinao, A. Peretto, Gas turbine fogging technology: a state-of-the-art review – part III: practical considerations and operational experience, J. Eng. Gas Turbines Power 129 (2007) 461–472.
[14] J. Vanderover, M.A. Oehlschlaeger, Ignition time measurements for methylcylcohexane- and ethylcyclohexane–air mixtures at elevated pressures, Int. J. Chem. Kinet. 41 (2009) 82–91.
[15] H.-P.S. Shen, J. Steinberg, J. Vanderover, M.A. Oehlschlaeger, A shock tube study of the ignition of *n*-heptane, *n*-decane, *n*-dodecane, and *n*-tetradecane, Energy & Fuels 23 (2009) 2482–2489.
[16] D.F. Davidson, D.R. Haylett, R.K. Hanson, Development of an aerosol shock tube for kinetic studies of low-vapor-pressure fuels, Combust. Flame 155 (2008) 108–117.
[17] C. Allen, T. Lee, Energetic-nanoparticle-enhanced combustion of liquid fuels in a rapid compression machine, AIAA-2009-0227, 2009.
[18] C.K. Law, Recent advances in droplet vaporization and combustion, Prog. Energy Combust. Sci. 8 (1982) 169–195.
[19] W.A. Sirignano, Fluid Dynamics and Transport of Droplets and Sprays, Cambridge University Press, Cambridge, UK, 1999.
[20] S.S. Sazhin, T. Kristyadi, W.A. Abdelghaffar, M.R. Heikal, Models for fuel droplet heating and evaporation: Comparative analysis, Fuel 85 (2006) 1613–1630.
[21] S.K. Aggarwal, H.C. Mongia, Multicomponent and high pressure effects on droplet vaporization, J. Eng. Gas Turb. Power 124 (2002) 248–255.
[22] S.K. Aggarwal, C. Yan, G. Zhu, Transcritical vaporization of a liquid fuel droplet in a supercritical ambient, Combust. Sci. Tech. 174 (2002) 103–130.
[23] H. Kim, N. Sung, The effect of ambient pressure on the evaporation of a single droplet and a spray, Combust. Flame 135 (2003) 261–270.
[24] C. Yan, S.K. Aggarwal, High-pressure droplet model for spray simulations, J. Eng. Gas Turb. Power 128 (2006) 482–492.
[25] F. Poplow, Numerical calculation of the transition from subcritical droplet evaporation to supercritical diffusion, Int. J. Heat Mass Transfer 37 (1994) 485–492.
[26] S. Aggarwal, G.S. Zhu, R.D. Reitz, Quasi-steady high-pressure droplet model for diesel sprays, SAE Paper 2000-01-0588, 2000.
[27] G.S. Zhu, S.K. Aggarwal, Transient supercritical droplet evaporation with emphasis on the effects of equation of state, Int. J. Heat Mass Transfer 43 (2000) 1157–1171.
[28] G.S. Zhu, R.D. Reitz, S.K. Aggarwal, Gas-phase unsteadiness and its influence on droplet vaporization in sub- and super-critical environments, Int. J. Heat Mass Transfer 44 (2001) 3081–3093.
[29] G.S. Zhu, S.K. Aggarwal, Fuel droplet evaporation in a supercritical environment, J. Eng. Gas Turbines Power 124 (2002) 762–770.
[30] V.R. Dushin, A.V. Kulchitskiy, V.S. Nerchenko, V.F. Nikitin, E.S. Osadchaya, Yu.G. Phylippov, N.N. Smirnov, Mathematical simulation for non-equilibrium droplet evaporation, Acta Astronautica 63 (2008) 1360–1371.
[31] E. Quandt, Water droplet evaporation in air during compression in a gas turbine engine, NSWCCD-TM-80-96/96, Naval Surface Warfare Center, Carderock Div., Bethesda, MD, 1996.
[32] Q. Zheng, Y. Sun, S. Li, Y. Wang, Thermodynamic analysis of wet compression process in the compressor of gas turbine, J. Turbomach. 125 (2003) 489–496.
[33] K. Zhang, S. Zou, W. Pan, F. Xue, Experimental investigation and numerical simulation of liquid droplet vaporization in a compression system with wet compression, Proc. ASME Power, Power2004-52029, 2004.
[34] A.J. White, A.J. Meacock, An evaluation of the effects of water injection on compressor performance, J. Eng. Gas Turbines Power 126 (2004) 748–754.
[35] J.-S. Kang, B.-J. Cha, S.-S. Yang, Thermodynamic and aerodynamic meanline analysis of wet compression in a centrifugal compressor, J. Mech. Sci. Tech. (KSME Int. J.) 20 (2006) 1475–1482.
[36] I. Roumeliotis, K. Mathioudakis, Evaluation of interstage water injection effect on compressor and engine performance, J. Eng. Gas Turbines Power 128 (2006) 849–856.
[37] K.-H. Kim, H. Perez-Blanco, Potential of regenerative gas-turbine systems with high fogging compression, Appl. Energy 84 (2007).
[38] M. Bagnoli, M. Bianchi, F. Melino, P.R. Spina, Development and validation of a computational code for wet compression simulation of gas turbines, J. Eng. Gas Turbines Power 130 (2008) 012004.
[39] X.Q. Liu, C.H. Wang, C.K. Law, Simulation of fuel droplet gasification in SI engines, J. Eng. Gas Turb. Power 106 (1984) 849–853.
[40] W.J. Sheu, N.C. Liou, Effect of temporal variation of pressure on vaporization of liquid droplets, Int. J. Heat Mass Transfer 42 (1999) 4043–4054.
[41] S.S. Goldsborough, C.J. Potokar, The influence of crevice flows and blow-by on the charge motion and temperature profiles within a Rapid Compression Expansion Machine used for chemical kinetic (HCCI) studies, SAE Paper 2007-01-0169, 2007.
[42] G. Mittal, M.P. Raju, C.-J. Sung, Computational fluid dynamics modeling of hydrogen ignition in a rapid compression machine, Combust. Flame 155 (2008) 417–428.
[43] S. Dooley, Autoignition measurements and a validated detailed kinetic model for the combustion of the model biodiesel: Methyl butanoate, PhD Dissertation, National University of Ireland, Galway, 2008.
[44] C.K. Westbrook, W.J. Pitz, O. Herbinet, H.J. Curran, E.J. Silke, A comprehensive detailed chemical kinetic reaction mechanism for combustion of *n*-alkane hydrocarbons from *n*-octane to *n*-hexadecane, Combust. Flame 156 (2009) 181–199.
[45] D.R. Caudwell, J.P.M. Trusler, V. Vesovic, W.A. Wakeham, The viscosity and density of *n*-dodecane and *n*-octadecane at pressures up to 200 MPa and temperatures up to 473 K, Int. J. Thermophys. 25 (2004) 1572–9567.
[46] E.R. Ritter, J.W. Bozzelli, THERM: Thermodynamic property estimation for radicals and molecules, Int. J. Chem. Kinet. 23 (1991) 767.
[47] V. Rùzicka, E.S. Domalski, Estimation of the heat capacities of organic liquids as a function of temperature using group additivity, I. Hydrocarbon compounds, J. Phys. Chem. Ref. Data 22 (1993) 597–619.
[48] D. Roy, G. Thodos, Thermal conductivity of gases. Hydrocarbons at normal pressures, Ind. Eng. Chem. Fundam. 7 (1968) 529–534.
[49] D. Roy, G. Thodos, Thermal conductivity of gases. Organic compounds at atmospheric pressure, Ind. Eng. Chem. Fundam. 9 (1970) 71–79.
[50] B.E. Poling, J.M. Prausnitz, J.P. O'Connell, The Properties of Gases and Liquids, fifth ed., McGraw-Hill, New York, 2001.
[51] B.I. Lee, M.G. Kessler, A generalized thermodynamic correlation based on three-parameter corresponding states, AIChE J. 21 (1975) 510.
[52] G.L. Hubbard, V.E. Denny, A.F. Mills, Droplet evaporation: effects of transients and variable properties, Int. J. Heat Mass Transfer 18 (1975) 1003–1008.
[53] T.H. Chung, M. Ajlan, L.L. Lee, K.E. Starling, Generalized multiparameter correlation for nonpolar and polar fluid transport properties, Ind. Eng. Chem. 27 (1988) 671–679.
[54] S. Takahashi, Preparation of a generalized chart for the diffusion coefficients of gases at high pressures, J. Chem. Eng. 6 (1974) 417–420.
[55] R.B. Bird, W.E. Stewart, E.N. Lightfoot, Transport Phenomena, John Wiley and Sons, New York, 1960.
[56] D.Y. Peng, D.B. Robinson, A new two-constant equation of state, Ind. Eng. Chem.: Fund. 15 (1976) 59–64.
[57] I.L. Byung, G.K. Michael, A generalized thermodynamic correlation based on three-parameter corresponding states, AIChE J. 21 (1975) 510–527.
[58] L.P. Filippov, Thermal conduction in solutions of associated liquids: thermal conduction of 50 organic liquids, Chem. Abstr. 50 (1956) 8276.
[59] K. Nakanishi, Prediction of diffusion coefficients of nonelectrolytes in dilute solution based on generalized Hammond-Stokes plot, Ind. Eng. Chem Fundam. 17 (1978) 253–256.
[60] G.H. Thomson, K.R. Brobst, R.W. Hankinson, An improved correlation for densities of compressed liquids and liquid mixtures, AIChE J. 28 (1982) 671–676.
[61] H.L. Finke, M.E. Gross, G. Waddington, H.M. Huffman, Low-temperature thermal data for the nine normal paraffin hydrocarbons from octane to hexadecane, J. Am. Chem. Soc. 76 (1954) 333–341.
[62] M.S. Benson, P.S. Snyder, J. Winnick, Heat capacities of liquid n-alkanes at elevated pressures, J. Chem. Therm. 3 (1971) 891–898.
[63] D. Bessieres, H. Saint-Guirons, J.-L. Dairdon, High pressure measurement of n-dodecane heat capacity up to 100MPa. Calculation from equations of state, High Pressure Research 18 (2000) 279–284.
[64] H. Kashiwagi, M. Oishi, Y. Tanaka, H. Kubota, T. Mikita, Thermal conductivity of fourteen liquids in the temperature range 298–373 K, Int. J. Thermophys. 3 (1982) 101–116.
[65] Y. Tanaka, Y. Itani, H. Kubota, T. Makita, Thermal conductivity of five normal alkanes in the temperature range 283–373 K at pressures up to 250 MPa, Int. J. Thermophys. 9 (1988) 331–350.
[66] H.N. Maia de Oliveira, F.W. Bezzera Lopes, A.A. Dantas Neto, O. Chiavone-Filho, Vapor-liquid equilibria for pentane + dodecane and heptane + dodecane at low pressures, J. Chem. Eng. Data 47 (2002) 1384–1387.
[67] E. Morawetz, Enthalpies of vaporization of *n*-alkanes from C12 to C20, J. Chem. Therm. 4 (1972) 139–144.
[68] K. Sasse, J. Jose, J.-C. Merlin, A static apparatus for measurement of low vapor pressures. Experimental results on high molecular-weight hydrocarbons, Fluid Phase Equilib. 42 (1988) 287–304.
[69] R.L. Smith Jr., A.S. Teja, W.B. Kay, Measurement of critical temperatures of thermally unstable *n*-alkanes, AIChE J. 33 (1987) 232–238.
[70] R.A. Mustafaev, Izv. Vyssh. Uchebn. Zaved. Neft Gaz 16 (1973) 71–74.